PCCP

Accepted Manuscript

ROYAL SOCIETY OF CHEMISTRY

www.rsc.org/pccp

Journal Name

ARTICLE

Thermoresponsive gold nanoshell @ mesoporous silica nano-assemblies: a XPS / NMR survey

Received 00th January 20xx,
Accepted 00th January 20xx

DOI: 10.1039/x0xx00000x

www.rsc.org/

S. Soulé,[a] J. Allouche,[a] J.-C. Dupin,*[a] C. Courrèges,[a] F. Plantier,[b] W.-S. Ojo,[c] Y. Coppel,[d] C. Nayral,[c] F. Delpech[c] and H. Martinez[a]

This work provides a detailed study about the physico-chemical characterization of a mechanized silver-gold alloy@mesoporous silica shell/pseudorotaxane nano-assembly using two main complementary techniques: XPS and NMR (liquid- and solid-state). The pseudorotaxane nanovalve is composed of a stalk (N-(6-aminohexyl)-aminomethyltriethoxysilane)/ macrocycle (cucurbit[6]uril (CB6)) complex anchored to the silica shell leading to a silica/nanovalve hybrid organic-inorganic interface that has been fully characterized. The stalk introduction in the silica network was clearly demonstrated by XPS measurements, with the Si2p peak shifting to lower energy after grafting, and through the analysis of the C1s and N1s core peaks, which indicated the presence of CB6 on the nanoparticle surface. For the first time, the complex formation on nanoparticles was proved by high speed ^{1}H MAS NMR experiments. However, these solid state NMR analyses have shown that the majority of the stalk does not interact with the CB6 macrocycle, when formulated in powder after removing the solvent. This can be related to the large number of possible organizations and interactions between the stalk, the CB6 and the silica surface. These results highlight the importance of using a combination of adapted and complementary highly sensitive surface and volume characterization techniques to design tailor-made hybrid hierarchical structured nano-assemblies with controlled and efficient properties for potential biological purposes.

Introduction

Over the past decade, mechanized silica nanoparticles have attracted a great attention promising high potentialities in the field of cancer therapy especially for drug delivery purposes.[1,2] These organic-inorganic hybrid materials are based on a mesoporous silica framework functionalized with stimulus-responsive (pH, redox potential, light, magnetic field) mechanically interlocked molecules.[3–6]

In addition, recent developments in Nanomedicine helped by a multidisciplinary way involving chemists, biologists and physicists have reached a new dimension with the design of multifunctional nanomaterials. For instance, “theranostic” agents have recently emerged as promising entities able to combine simultaneously therapeutic and diagnostic functions.[7–11] More particularly, core-shell nanoparticles have been of great interest since they offer the possibility to combine several functions in a one single unit with generally stimuli-responsive properties.

Especially, the group of Zink has demonstrated the possibility to design photoresponsive nanomachines by including a gold core into mechanized silica nanoparticles.[12] The plasmonic properties of the gold core combined with the drug-carrying capability of the mesoporous silica shell result in a temperature triggered drug controlled release nanosystem.

Our group has recently shown the possibility to design a similar model architecture based on gold nanoshell@mesoporous silica shell nanoparticles with a radial pore orientation.[13] Gold nanoshells appear to be more adapted for living systems since their absorption can be tuned in the near-infrared (NIR) corresponding to the biological window.

In such mechanized silica nanoparticles, two organic moieties, involved in the formation of supramolecular nanomachines, are combined to the silica material to provide suitable and activable pore-gate keeping nanovalves on nanoparticles surface: a linear stalk as guest, anchored to the silica surface, and gating rings as host macrocycles which encircle the stalks. The two species are linked mechanically forming a complex via weak supramolecular interactions which can be disrupted by external stimuli (eg. pH variation, plasmonic photothermal activation).

[a] Institut des Sciences Analytiques et de Physico-Chimie pour l’Environnement et les Matériaux, Université de Pau et des Pays de l’Adour, Hélioparc, 2 av. Président Angot, F-64053 Pau, France. E-mail: jean-charles.dupin@univ-pau.fr
[b] LFC-R – Laboratoire des Fluides Complexes et leurs Réservoirs, Université Pau et Pays Adour, CNRS, TOTAL - UMR 5150 –BP 1155 – PAU, F-64013, France.
[c] Université de Toulouse; INSA, UPS, CNRS; LPCNO (Laboratoire de Physique et Chimie des Nano-Objets), 135 avenue de Rangueil, F-31077 Toulouse, France.
[d] Laboratoire de Chimie de Coordination du CNRS (LCC), 205 route de Narbonne, F-31077 Toulouse cedex 4, France.
† Electronic Supplementary Information (ESI) available. See DOI: 10.1039/x0xx00000x

The control of such mechanization at nanoscale involving hybrid organic-inorganic and organic-organic interfaces requires a fine-tuning of synthesis conditions that cannot be realized without a complete, suitable and efficient morphological and physico-chemical characterization of materials. Moreover, such characterization investigations have to be done within a framework of a general strategy involving the use of adapted complementary techniques to corroborate and confront morphological, structural and chemical information of different natures and extent. This key point is often under considered in favor of the demonstration of the successful design of new mechanized nanosystems involving decorative organic molecules on nanoparticles surface. In addition, concerning stalk/macrocycle pseudorotaxane based materials, various techniques are used to evidence their existence onto nanoparticles. In fact, the multi-step functionalization is commonly approached with Fourier Transform Infrared Spectroscopy (FTIR). C-H stretching vibration modes attest of the introduction of stalk and carbonyl stretching band generally confirms the presence of CB6 macrocycle.[14–17] Solid state NMR is also widely used, particularly ^{29}Si and ^{13}C CP-MAS to attest of stalk grafting.[12,16–18] To our knowledge, one main paper reports the stalk introduction in the framework of nanoparticles by X-ray Photoelectron spectroscopy (XPS) with the analysis of C1s and N1s spectra.[16] Moreover, thermogravimetric analysis provides quantitative information about the functionalization[15–17]. However, a detailed physico-chemical analysis and description of the complex formation on nanoparticles surface are still lacking. This is mainly due to the difficulty of discriminating complex chemical interactions and information that occurs at hybrid organic-inorganic interfaces (covalent and weak bonding, grafting density, physico-chemical adsorption…) without using suitable complementary techniques able to characterize materials at nanoscale.

In this context, this prospective work is focused on the physico-chemical characterization of some model gold nanoshells@mesoporous silica nanoparticles and particularly on their functionalization by organic nanovalves. Parallely to the structural and morphological characterization of materials by TEM and nitrogen adsorption analyses, our strategy consists in using two complementary techniques: X-ray Photoelectron Spectroscopy and multinuclear solution- and solid-state NMR to probe both the surface modification of nanoparticles as well as the interaction coming originally from nanovalves formation. For the first time, we have investigated the local environment of linear stalk anchored on the mesoporous silica shell and we pointed out in this work a way to chemically attest of a macrocycle-based pseudorotaxane formation on nanoparticles.

Experimental

Chemicals

Silver nitrate ($AgNO_3$, Sigma, >99%), tetrachloroauric acid trihydrate ($HAuCl_4.3H_2O$, Sigma, >99.9%), tri-sodium citrate (Fisher, >99%), Polyvinylpyrrolidone (PVP, 10.000 g/mol, Sigma), sodium hydroxide (Fisher, >98%), tetraethylorthosilicate (TEOS, Sigma, >98%), ammonia (Sigma, 28 wt.%), cetyltrimethylammonium bromide (CTAB, Sigma, >98%), anhydrous ethanol (Sigma, >99.5%), isopropanol (Sigma, >99%), N,N-Dimethylformamide (anhydrous, Sigma, 99,8 %), N-(6-aminohexyl)aminomethyltriethoxysilane (stalk, ABCR, >95%), sodium chloride (NaCl, >98%), cucurbit[6]uril hydrate (CB6, Sigma) were used as received without further purification.

Synthesis of functionalized core-shell nanoparticles

First, the synthesis of core-shell silver-gold alloy nanoshell@mesoporous silica nanoparticles (NS@mSi) was performed following our recent published procedure.[13]

The functionalization of NS@mSi nanoparticles by nanovalves was performed using a procedure developed by Thomas *et al.*[19] but adapted to our case. It consists in a two steps process where an organic stalk (N-(6-aminohexyl)amino-methyltriethoxysilane) was firstly grafted on particles. Secondly, pore closing was achieved by complexation of the organic pore-gate keeper macrocycle cucurbit[6]uril (CB6) with the stalk (scheme 1).

Stalk grafting on silica shell (NS@mSi-stalk). First, a solution (**1**) containing 236 µl of N-(6-aminohexyl)-aminomethyltriethoxysilane in 5 ml of dried dimethyl-formamide was prepared. Then, NS@mSi were dispersed in dried dimethylformamide (30 mg, 20 ml (**2**)) and stirred at room temperature. Afterwards, 0.5 ml of **1** was added in **2** and the reaction was conducted overnight at 80°C under magnetic stirring. Finally the solution was filtered and washed several times with ethanol.

Pore closing. 30 mg of NS@mSi-stalk were dispersed in 5 ml of deionized water (**3**). 7 ml of an aqueous solution of cucurbit[6]uril (75 mg) and sodium chloride (65 mg) was added to **3**. The solution was kept under magnetic stirring during three days. Finally, nanoparticles were recovered after several centrifugation/washing cycles with water.

Synthesis of reference systems

SiO_2 nanoparticles. A solution of 4 ml of water, 20 ml of isopropanol, 0.5 ml of concentrated ammonia and 10 µl of TEOS was prepared and stirred 2 h leading to SiO_2 dense cores

Scheme 1 Illustration of the two step nanovalves functionalization of NS@mSi particles

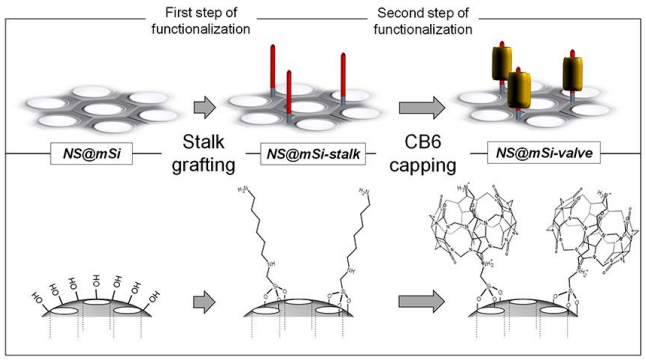

in a first step. In a next step, a mesoporous silica shell was grown on particles by adding 0.06 g of CTAB solubilized in 56 ml of deionised water followed by 107 µl of TEOS. The solution was stirred overnight before being filtered and washed several times to recover the SiO_2 nanoparticles. CTAB was finally removed from the pores by redispersing the nanoparticles in an ethanol/HCl (two drops of 36 wt.%) solution overnight followed by others filtration/washing cycles.

Stalk$^+$ [$(CH_3CH_2O)_3SiCH_2NH_2(CH_2)6NH_3]Cl_2$. 234 mg of stalk were added to 5 ml of pentane. Next, 5 ml of a solution of $HCl.Et_2O$ (1M) was slowly introduced under stirring. After 2h, the precipitate was recovered by filtration and washed 3 times with 10 ml of pentane. Finally, the solid was dried under vacuum during 4h.

Stalk$^+$/CB6. 7 ml of an aqueous solution of CB6 (100 mg) and sodium chloride (85 mg) was first prepared and stirred during 5h. After that, the solution was added to an aqueous solution of stalk$^+$ (45 mg). The final solution was kept under magnetic stirring during three days. The complex was recorded by filtration after precipitation with acetone and several washing with ethanol.

Characterization

Morphological and structural characterization. Morphology of nanoparticles was evaluated by transmission electron microscopy (TEM). The images were recorded with a Philips CM 200 (200 kV) instrument equipped with a LaB_6 source. The samples dispersed in ethanol were dropped onto a carbon copper grid and dried before analysis.

Nitrogen adsorption and desorption isotherms of the nanoparticles were measured at 77 K and were carried out with a Micromeritics ASAP 2020 instrument. Results were analyzed in terms of specific area by BET method[20] and total pore volume as well as pore size distribution were calculated by using a density functional theory approach.[21]

Chemical characterizations

X-ray Photoelectron Spectroscopy (XPS). XPS measurements were performed on a Thermo K-alpha spectrometer with a hemispherical analyzer and a microfocused (400µm diameter microspot) monochromated radiation (Al Kα, 1486.6 eV) operating at 72 W under a residual pressure of 1.10^{-9}mbar. The pass energy was set to 20 eV. Charge effects were compensated by the use of a dual beam charge neutralization system which combines low energy electrons and Ar^+ ions to provide efficient charge compensation. Spectra were mathematically fitted with Casa XPS software© using a least squares algorithm. The background in narrow range spectra was accommodated by a non-linear Shirley function.[22] The experimental curves were fitted using a combination of Gaussian (70%) and Lorentzian (30%) distributions. The binding energy scale was calibrated from the hydrocarbon contamination using the C 1s peak at 285.0 eV. Quantification was performed on the basis of Scofield's relative sensitivity factors.[23]

Nuclear Magnetic Resonance Spectroscopy (NMR). Solid-state NMR experiments were recorded on a Bruker Avance 400 spectrometer equipped with a 4 mm and 1.3 mm probe. Samples were spun at 10 kHz or 60 kHz at the magic angle. For ^{1}H MAS and ^{29}Si MAS single pulse experiments were performed with recycle delays of 5 s and 60 s, respectively. ^{13}C-CP/MAS and ^{29}Si-CP/MAS spectra were recorded with a recycle delay of 3 s and contact times of 2 ms and 3 ms respectively. The 2D ^{1}H-^{1}H double-quantum (DQ) MAS experiments were recorded with the back-to-back (BABA) sequence[24] at a spinning frequency of 60 kHz.

1D and 2D ^{1}H NMR experiments in liquid state were recorded on a Bruker Avance 500 spectrometer equipped with a 5 mm triple resonance inverse Z-gradient probe (TBI ^{1}H, ^{31}P, BB). The 2D ROESY measurements were done with a mixing time of 300 ms. All diffusion measurements were made using the stimulated echo pulse sequence with bipolar gradient pulses. The diffusion delay (Δ) was set to 150 ms and the gradient pulse duration (δ) to 1.5 ms in order to obtain 1-5% residual signal with maximum gradient strength. The recycle delay was adjusted to 3 s. Rectangular shapes were used for the gradients and a linear gradient ramp with 16 or 32 increments between 2% and 95% was applied for the diffusion relevant gradients. The strength of the gradient (56.0 Gauss/cm at a current of 10A) was calibrated by measuring the self diffusion of the residual HDO signal in a 100 % D_2O sample at 298K (1.90 x 10^{-9} $m^2.s^{-1}$). For 2D diffusion ordered spectroscopy (DOSY), after Fourier transformation and baseline correction, the diffusion dimension was processed with the Bruker Topspin software package DOSY. All chemical shifts for ^{1}H, ^{13}C and ^{29}Si are relative to TMS using the ^{1}H signal of HOD (4.87 ppm at 293K) for liquid state NMR. For solid state NMR, H_2O for ^{1}H (4.87 ppm at 293K), adamantane for ^{13}C (38.48 ppm) and tetrakis(trimethylsilyl)silane for ^{29}Si (−9.8 and −125.2 ppm) were used as secondary external standards.

Results and Discussion

Morphological and structural characterization

TEM pictures (Fig. 1a, b) of the silver-gold alloy nanoshell@mesoporous silica nanoparticles (NS@mSi) first highlight the well-defined core-shell structure of particles consisting in silver-gold alloy cores[25] coated with a mesoporous silica shell. The average particles diameter was approximately 440 ± 30 nm.

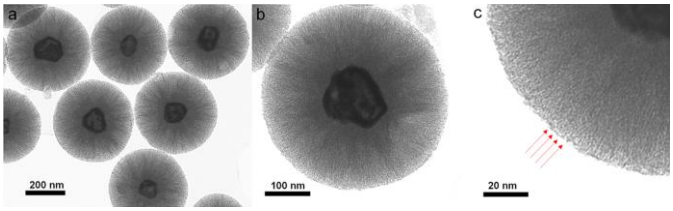

Fig. 1 Low and high magnification TEM pictures of core–shell NS@mSi nanoparticles

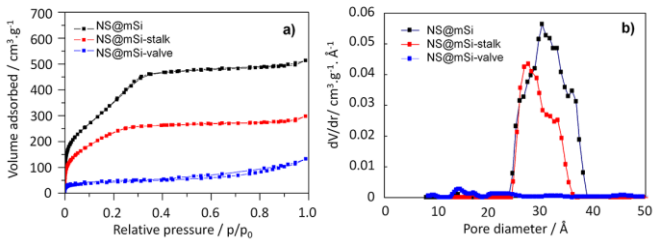

Fig. 2 Comparison of a) nitrogen adsorption/desorption isotherms at 77K and b) pore size distribution of studied materials

Table 1 Surface area and total pore volume of NS@mSi, NS@mSi-stalk, NS@mSi-valve calculated from N_2 adsorption-desorption isotherms

Nanomaterials	Surface area / $m^2.g^{-1}$	Total pore volume / $cm^3.g^{-1}$
NS@mSi	1460	0.72
NS@mSi-stalk	860	0.40
NS@mSi-valve	150	0.14

The silica shell exhibits a radial pore orientation (Fig. 1c) and the thickness is evaluated to 160 ± 10 nm is in agreement with the synthetic procedure provided in our recent publication.[13] As expected and illustrated in scheme 1, each of the two steps of the NS@mSi nanoparticles functionalization by nanovalves leads to a significant decrease of both surface area and total pore volume. Indeed, the surface area and the total pore volume (deduced respectively from the corrected Brunauer-Emmet-Teller[20] (BET) equation and Density Functional Theory[21] (DFT) approach) decrease from 1460 to 150 $m^2.g^{-1}$ and from 0.72 to 0.14 $cm^3.g^{-1}$ respectively (Table 1).

In addition, the pore size distributions of NS@mSi, NS@mSi-stalk and NS@mSi-valve were calculated and are presented in Figure 2. For NS@mSi and NS@mSi-stalk materials, the distribution shows a broad peak in 24 - 38 Å pore range. However, the absence of pore size distribution for NS@mSi-valve clearly indicates that the complexation of the organic macrocycle with the stalk partially closes the mesoporous network. These results are in agreement with the evolution of the surface area and the total pore volume decrease and give a first assessment of the effective organic functionalization on NS@mSi. The precise understanding of such complex nano-assembly needs more detailed investigations. Actually the nature of physico-chemical mechanisms occurring at the hybrid organic-inorganic interface could then be probed.

XPS characterization

Analysis of silica nanoparticles, stalk$^+$, CB6 and stalk$^+$/CB6 materials

A preliminary study of several references: SiO_2 nanoparticles, stalk$^+$, CB6 and stalk$^+$/CB6 complex has been done by XPS. The main objective is to provide chemical a data set of binding energies associated to their corresponding chemical environments. The related results of these reference compounds are reported in table 2. For SiO_2 nanoparticles, XPS analysis evidence the presence of carbon contamination (8.1 at.%), oxygen (58.0 at.%) and silicon (33.9 at.%).

Table 2. XPS binding energies and atomic percentages of C1s, Cl2p, N1s, O1s and Si2p core peaks for SiO_2 nanoparticles, stalk+, CB6 and stalk+/CB6. [a] In brackets are indicated the full width at half-maximum of peaks.

	SiO_2 nanoparticles		Stalk$^+$		CB6		Stalk$^+$/CB6	
Core peaks	**BE / eV (fwhm / eV)[a]**	**at. %**	**BE / eV (fwhm / eV)[a]**	**at. %**	**BE / eV (fwhm / eV)[a]**	**at. %**	**BE / eV (fwhm / eV)[a]**	**at. %**
C1s	285.0 (1.7)	5.2	285.0 (1.3)	42.5	285.0 (1.8)	17.7	285.0 (1.4)	16.0
	286.2 (1.7)	1.6	286.2 (1.3)	15.0			286.0 (1.4)	5.7
	287.4 (1.7)	1.0	287.0 (1.3)	5.5	287.4 (1.8)	27.9	287.6 (1.4)	23.6
	288.9 (1.7)	0.3	288.9 (1.3)	1.7	289.0 (1.8)	16.1	289.2 (1.4)	13.3
Total at.%		**8.1**		**64.7**		**61.7**		**58.6**
Cl $2p_{3/2}$	-		197.7 (1.2)	5.5	-		197.4 (1.4)	1.0
Cl $2p_{1/2}$	-		199.3 (1.2)	2.7	-		199.1 (1.4)	0.5
Total at.%				**8.2**				**1.5**
N1s	-		399.8 (1.5)	0.5				
	-				400.1 (1.8)	24.6	400.3 (1.5)	22.1
	-		401.7 (1.5)	6.9			402.0 (1.5)	1.8
Total at.%				**7.4**		**24.6**		**23.9**
O1s					531.6 (1.8)	12.1	531.8 (1.5)	10.7
	533.4 (1.9)	54.5	532.6 (1.4)	12.1	533.3 (1.8)	1.6	532.6 (1.6)	3.0
	534.9 (1.9)	3.5	533.9 (1.4)	1.1			533.7 (1.6)	0.8
Total at.%		**58.0**		**13.2**		**13.7**		**14.5**
Si $2p_{3/2}$	104.1 (1.8)	22.6	102.5 (1.3)	4.3	-		102.5 (1.7)	1.0
Si $2p_{1/2}$	104.7 (1.8)	11.3	103.2 (1.3)	2.2	-		103.1 (1.7)	0.5
Total at.%		**33.9**		**6.5**				**1.5**

The Si2p spectrum (see Fig. S1a†) exhibits the two spin-orbit splitting $2p_{3/2}$ and $2p_{1/2}$ contributions with binding energies at respectively 104.1 and 104.7 eV which are typical values of SiO_2.[26]

In addition, two different components have been identified on the O1s peak (see Fig. S1b†): one located at 533.4 eV corresponding to silica and another one at 534.9 eV assigned to silanols groups.[27] Finally, the O/Si ratio was found to be 1.7.

The two nanovalve moieties and for the first time, the host-guest stalk$^+$/CB6 complex were also analyzed by XPS.

Concerning the protonated form of stalk called stalk$^+$, 64.7 at. % of carbon were detected and the C1s spectrum (Fig. 3a) exhibits four distinctive environments.

The first component at 285.0 eV corresponds to C-C/C-H bonds of the aliphatic chain and also to hydrocarbon of contamination. The second component at 286.2 eV is assigned to both C-N bonds and ethoxy groups while the two other components at higher energies correspond to residual contamination from synthesis.

Quantitative analysis gives 6.5 % of Si and the Si2p core peak binding energy (102.5-103.2 eV) is characteristic of alkyltriethoxysilane ($(EtO)_3Si$-C).[28] The corresponding oxygen environment is found at 532.6 eV (12.1 at. %). The other oxygen component at 533.9 eV is associated with some hydrolyzed ethoxy groups (1.1 at. %). Finally, the N1s spectrum (Fig. 3b) displays two components at 399.8 eV and 401.7 eV respectively assigned to amine and ammonium groups of the stalk composition.[29–31]

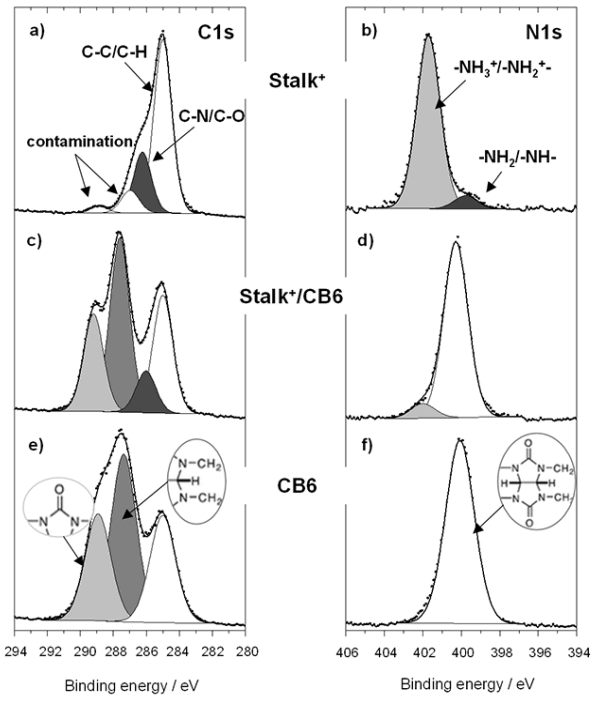

Fig. 3 C1s and N1s spectra of some references: stalk$^+$ (a, b), stalk$^+$/CB6 (c, d) and CB6 (e, f)

The quantitative data clearly show the abundance of ammonium groups (6.9 at. %) compared to the amine (0.5 at. %) confirming that the stalk is predominantly in its protonated form. XPS analysis also indicates the presence of chloride (8.2 at. %) coming from the synthesis of stalk$^+$ reference sample that involves acidification with HCl. Chloride then plays the role of counterion of the ammonium groups as confirmed by quantitative data.

For the CB6 macrocycle, the C1s spectrum (Fig. 3e) clearly shows the presence of three chemical environments (61.7 total at. %). The first component (C1) at 285.0 eV, corresponds to hydrocarbon of residual contamination present in the commercial organics (C-C and C-H bonds). The other two, located at 287.4 (C2) and 289.0 eV (C3), are assigned respectively to alkylamine (N-**C**H_2-N/N-(**C**H)-N) and carbamide (N-(**C**=O)-N) environments. The N1s spectrum (Fig. 3f) confirms the single nitrogen state at 400.0 eV (N1) from carbamide nitrogen group. The O1s signal (see Fig. S2†) attests of the previous chemical environment with a component located at 531.6 eV (O1) for oxygen atoms of CB6 (N-(C=**O**)-N) and a small intensity component at 533.3 eV (O2) attributed to water of hydrate composition.

The quantitative data are very close to the stoichiometry of CB6 with a C2/C3/N1/O1 atomic composition of 1.0/0.6/0.9/0.4 (1.0/0.5/1.0/0.5 theoretically).

Finally, for the stalk$^+$/CB6 complex, the C1s core peak (Fig. 3c) presents four components: the first one at 285.0 eV is attributed to C-C and C-H bonds due to alkyl chain of stalk but also to small amount of contamination. The second component at 286.0 eV is both associated to C-N stalk bonds and residual traces of oxidized carbon. The deconvolution also clearly evidences two components at higher energy, 287.6 and 289.2 eV, associated to the CB6 macrocycle as reported above.

Concerning the N1s spectrum (Fig. 3d), the core peak fits into two components. The most important one, located at 400.3 eV, includes both carbamide nitrogen contribution of CB6 and stalk amine groups because these two contributions can not be energetically separated.

On the other hand, the less intense component of the N1s signal at 402.0 eV is assigned to the stalk ammonium groups as previously shown in Figure 3b.

As expected, we also point out that CB6 signature dominates both C1s and N1s spectra due to its number of carbon and nitrogen atoms (e.g. 36 carbons atoms and 24 nitrogen atoms) more important than for the stalk (e.g. 7 carbon atoms and 2 nitrogen atoms). The quantification data agree with the stoichiometry of CB6. The ratio N1/N2 between the atomic nitrogen percentages of CB6 (N1) and stalk (N2) is equal to 12 for the reference stalk$^+$/CB6 system, in accordance with the theory (the interaction between one stalk molecule (2 nitrogen atoms) and one CB6 macrocycle (24 nitrogen atoms)).

Analysis of hybrid gold nanoshell@silica nanoparticles

After a complete characterization of reference materials, XPS analyses were performed on NS@mSi, NS@mSi-stalk and NS@mSi-valve for which the binding energies and quantitative data are reported in table 3.

As previously reported, the $Si2p_{3/2}$ component of NS@mSi (Fig. 4c) is found at 104.0 eV in accordance with SiO_2 reference nanoparticles. Additionally, the O1s spectrum (see Fig. S3†) displays the two components at 533.5 eV and 534.8 eV corresponding to SiO_2 and silanol environments and the O/Si atomic ratio is of 1.7 as for the reference SiO_2.
Then, the study of quantitative data allows to point out the effective surface functionalization that can be deduced from the evolution of atomic percentages.

Table 3. XPS binding energies and atomic percentages of C1s, N1s, O1s and Si2p core peaks for NS@mSi, NS@mSi-stalk and NS@mSi-valve. [a] In brackets are indicated the full width at half-maximum of peaks.

	NS@mSi		NS@mSi-stalk		NS@mSi-valve	
Core peaks	**BE / eV (fwhm / eV)[a]**	**at. %**	**BE / eV (fwhm / eV)[a]**	**at. %**	**BE / eV (fwhm / eV)[a]**	**at. %**
C1s	285.0 (1.5)	9.3	285.0 (1.7)	10.8	285.0 (1.8)	7.9
	286.1 (1.5)	3.3	286.4 (1.7)	4.9	286.0 (1.8)	3.8
	287.4 (1.5)	1.4	288.2 (1.7)	1.4	287.7 (1.8)	8.5
	289.1 (1.5)	0.5			289.3 (1.8)	4.7
Total at. %		**14.5**		**17.1**		**24.9**
N1s	-	-	399.9 (2.2)	1.5		
	-	-			400.4 (2.0)	7.8
	-	-	401.7 (2.2)	0.5	402.1 (2.0)	0.7
Total at. %				**2.0**		**8.5**
O1s	533.5 (1.8)	49.4	533.1 (1.8)	47.9	532.9 (2.1)	42.7
	534.8 (1.8)	4.2	534.3 (1.8)	3.6		
Total at. %		**53.6**		**51.5**		**42.7**
Si $2p_{3/2}$	104.0 (1.7)	21.3	103.5 (1.7)	19.6	103.4 (1.8)	16.0
Si $2p_{1/2}$	104.7 (1.7)	10.6	104.1 (1.7)	9.8	104.0 (1.8)	8.0
Total at. %		**31.9**		**29.4**		**24.0**

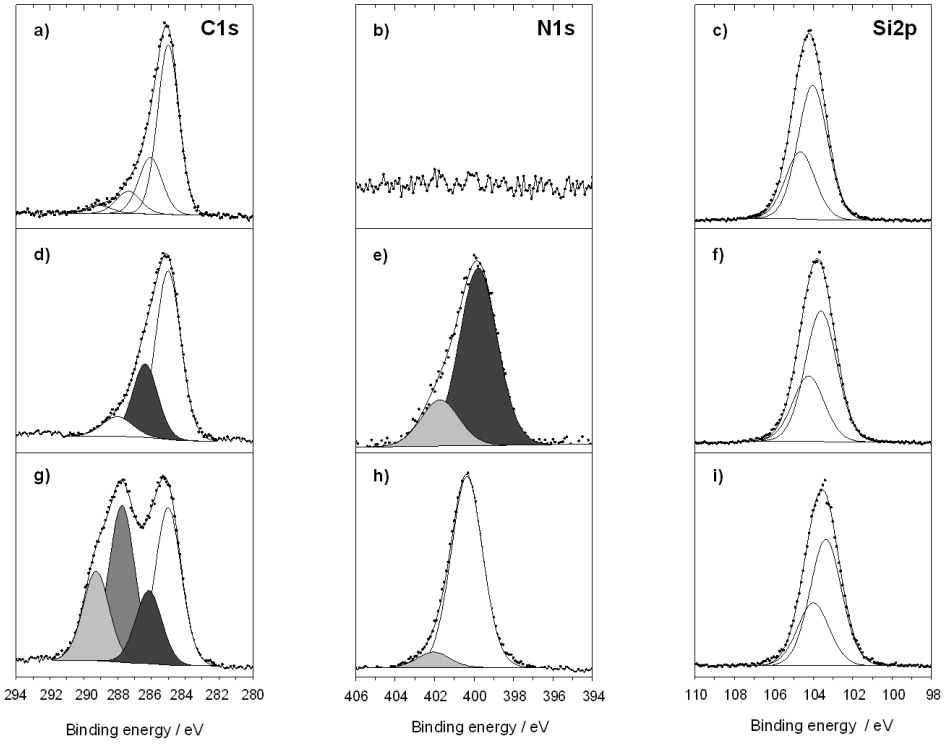

Fig. 4 C1s, N1s and Si2p spectra of NS@mSi (a, b, c), NS@mSi-stalk (d, e, f) and NS@mSi-valve (g, h, i)

Indeed, the amounts of silicon and oxygen decrease respectively from 31.9 at.% to 24.0 at.% and from 53.6 at.% to 42.7 at.% whereas those of carbon and nitrogen gradually increase from 14.5 at.% to 24.9 at.% and from 2.0 at.% (for NS@mSi-stalk) to 8.5 at.% respectively.

Considering the Si2p spectra, the $Si2p_{3/2}$ component after stalk grafting (Fig. 4f) (NS@mSi-stalk) is shifted to lower binding energies compared with NS@mSi. Actually the stalk grafting induces a modification of the chemical environment of surface silicon atoms. The less electronegative environment provided by the non-hydrolysable group of the stalk precursor decreases the binding energy of the $Si2p_{3/2}$ to 103.5 eV. This value corresponds to an average signal of SiO_2 (104.0 eV) and grafted stalk silicon atoms. The oxygen components, located at 533.1 and 534.3 eV, follow the same trend.

For the C1s spectra, the components assigned to aliphatic carbon increase slightly after stalk grafting (Fig. 4d). The C-O/C-N component at 286.4 eV also increases attesting to the effective functionalization. Finally, the detection of nitrogen signal reveals the presence of stalk on the surface. Moreover, the deconvolution of N1s spectra (Fig. 4e) evidences two components at 399.9 eV and 401.7 eV assigned to amine and ammonium groups as previously shown for the reference stalk$^+$ (Fig. 3b). However, we can note that the amine groups of stalk are predominantly in their basic form (not protonated) on the silica nanoparticles surface because the silanization was realized under anhydrous conditions and nanoparticles were dried after functionalization.[32,33]

After valve closing, the binding energy of Si2p peak for NS@mSi-valve (see table 3 and Fig. 4i) is not modified highlighting the preservation of the stalk functionalization.

The C1s and N1s spectra of NS@mSi-valve (Fig. 4g, h) are very similar to that of stalk$^+$/CB6 (Fig. 3c, d). Indeed, the C1s core peak presents the same four components at 285.0, 286.0, 287.7 and 289.3 eV. The N1s core peak fits into two components located at 400.4 eV corresponding to both carbamide groups of CB6 and amine groups of stalk, and 402.1 eV assigned to ammonium groups of stalk as previously discussed.

The stoichiometry of CB6 seems to be preserved even if the oxygen component of NS@mSi-valve can not be deconvoluted (see Fig. S4†). Concerning the ratio between the atomic nitrogen percentages of CB6 (N1) and stalk (N2), quite same result as stalk$^+$/CB6 is found (≈ 12/1).

In summary, the presence of both stalk and CB6 on particles as well as the effective functionalization of the silica shell have been demonstrated through XPS characterization. As reported in the literature, the driving forces that insure the CB6/stalk host-guest complexation is due to (i) ion-dipole interactions which promote binding of the cationic sites of organic guests and to (ii) a hydrophobic effect, which favors inclusion of organic residue.[34] However, these supramolecular interactions are too weak to induce a significant chemical shift in the XPS associated signals (e.g C1s and N1s peaks). To deeper investigate such interactions, NMR analyses were carried out.

NMR characterization

NMR analyses of stalk, CB6 and stalk$^+$/CB6 references

In the literature, the binding interactions of supramolecular assemblies involving positively charged organic guests and macrocycle hosts are generally evidenced by liquid-state ^{1}H NMR spectroscopy[18,35–38] and 2D ^{1}H-^{1}H ROESY[38,36] or NOESY[37] experiments. For the cucurbit[n]uril family, the inner cavity creates a ^{1}H NMR shielding region and a low frequency shift of -1 ppm for the guest hydrogen atoms residing inside is commonly observed.[39] Then, hydrogen atoms closer to the portal but still inside the cavity of CB are moderately shifted at low frequency (-0.1 to -0.8 ppm), and hydrogen outside the cavity undergo a moderate high frequency shift (up to +0.7 ppm) that weakens as the distance between the hydrogen and the portal increases.[40] Moreover, for the CB family, dynamic exchange processes between bound and free guests are often slow on the NMR time scale, thus allowing a direct observation of the free and bound guests simultaneously.[38,41]

Considering these results, we have decided to study the complex stalk$^+$/CB6 by ^{1}H liquid state NMR in order to evidence these specific proton shifts in our system.

The formation of inclusion complex between stalk and CB6 is first supported by ^{1}H NMR spectroscopy with shifts characteristic of the complex formation. Indeed, the hydrogen of stalk$^+$ interacting with CB6 (comparison between spectra in Fig. 5b and c) at positions *a* and *a'* are barely affected (-0.05 ppm) while the hydrogen at positions d undergo a moderate high frequency shift (+0.22 ppm). The hydrogens at positions *b*, *b'*, *c* and *c'* which are encapsulated into CB6, are strongly shifted to low frequency (-0.99 and -0.91 ppm, respectively). The complexation also perturbs the chemical shifts and the pattern of the CB6 proton resonances (comparison between spectra in Fig. 5a and b): each of the two free CB6 doublets H_1 and H_2 splits into several sets of doublets and the H_3 singlet undergoes a slight low frequency shift (-0.04 ppm) upon binding. This results probably from the presence of several complexes in equilibrium.

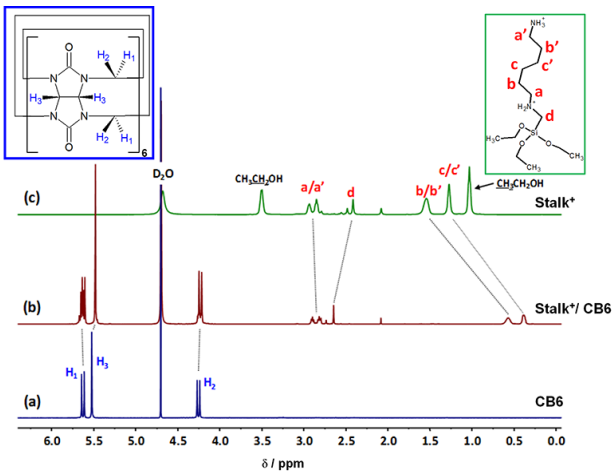

Fig. 5 ^{1}H NMR spectra of a) CB6, b) stalk$^+$/CB6 and of c) stalk$^+$

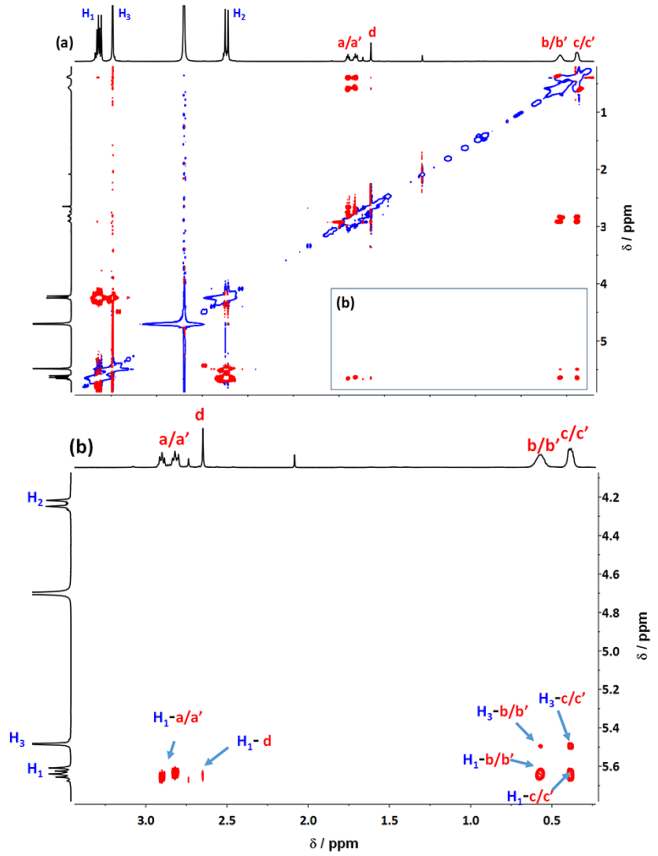

Fig. 6 2D ROESY NMR spectrum of stalk$^+$/CB6 in D_2O – a) full spectrum and b) expansion of the box area

Then, to provide additional evidence of the complex formation, 2D ROESY experiments were performed (Fig. 6). Cross-peaks are observed between the protons *a*, *a'*, *b*, *b'*, *c*, *c'* of stalk$^+$ and the H_1 protons of CB6. Furthermore, correlation peaks between the H_3 protons of CB6 with the aliphatic protons *b*, *b'*, *c* and *c'* can be observed, suggesting that the spatial distance between these protons is less than 5 Å.[38] In contrast, no correlation peaks exist between stalk$^+$ resonances and that of H_2 which are pointing outward.

This first study by liquid state ^{1}H NMR confirms the complex formation in solution but also points out the ^{1}H NMR shifts attesting to the inclusion of the stalk into CB6.

Additionally, the structure of the assembly can be confirmed by diffusion-ordered NMR spectroscopy (DOSY) measurements: from the decay of the resonance intensity as a function of field gradient strength of this NMR sequence, the diffusion coefficient of the species associated with the resonance can be obtained.[42,43]

The resonances of bound and free molecules can be separated along the diffusion dimension of the 2D spectrum if the ligand exchange rate is slow compared to the diffusion time scale. In our case, only one set of resonances for the ungrafted stalk and for CB6 is observed and the strong binding is firmly established by the identical self-diffusion coefficient (2.2×10^{-10} $m^2.s^{-1}$) observed for the two species (see Fig. S5†) which is significantly smaller than the free form ones (3.7×10^{-10} $m^2.s^{-1}$ and 2.5×10^{-10} $m^2.s^{-1}$ for stalk and CB6 respectively).

Solid-state Magic Angle Spinning (MAS) NMR characterization of functionalized hybrid nanoparticles

First, cross-polarization (CP) magic-angle spinning (MAS) ^{29}Si NMR was used in order to confirm the stalk grafting on the surface of nanoparticles. The spectra of the NS@mSi and NS@mSi-stalk are shown in Figure 7. In both cases, intense resonances can be observed at -91, -101 and -110 ppm which can be attributed to the Q-type silicon atoms (i.e., corresponding to silicon atoms forming four Si-O bonds): Q^2 ($Si(OSi)_2(OR)_2$, -91 ppm), Q^3 ($Si(OSi)_3OR$, -101 ppm), and Q^4 ($Si(OSi)_4$, -110 ppm with R = H, Et, or negative charge). The signal associated with T substructure silicon (i.e., corresponding to silicon atoms forming three Si–O bonds and one Si–C bond) around -70 ppm for the grafted stalk molecules is very weak. This result implies that the amount of T-type silicon atoms is very low compared to that of the Q-type silicon atoms (below the detection threshold i.e. typically less than 1%). In fact, considering the SiO_2 shell thickness of particles, the ratio between the numbers of volume and surface silicon atoms is very high suggesting that few silicon atoms are involved in the stalk grafting.[12,44]

CP-MAS ^{13}C NMR spectroscopy was then carried out to confirm the functionalization of stalk and evidence the presence of CB6. The assignments given in Figure 8 were done by comparison with the spectra of stalk$^+$ and of CB6 reference samples (see Fig. S6, S7†).

The resonances in the range of 26-51 ppm are due to methylene groups *b*, *b'*, *c*, *c'*, *d*, *a'* and *a* of stalk. Several signals are observed for *a'* peak, in both NS@mSi-valve and stalk$^+$ spectra (see Fig. S6†), which can be explained by the presence of different structural forms of the stalk grafted to NS@mSi.[16,31,45]

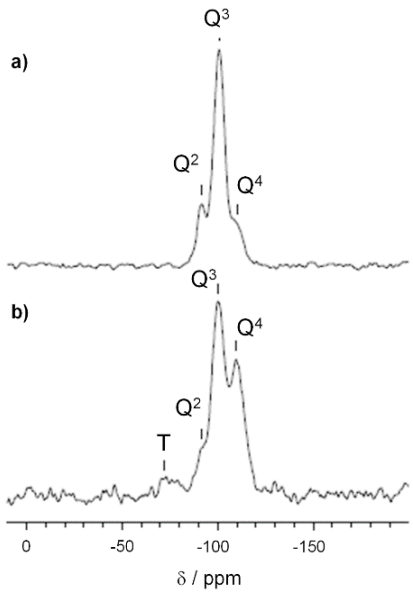

Fig. 7 CP-MAS ^{29}Si NMR spectrum of a) NS@mSi and b) NS@mSi-stalk

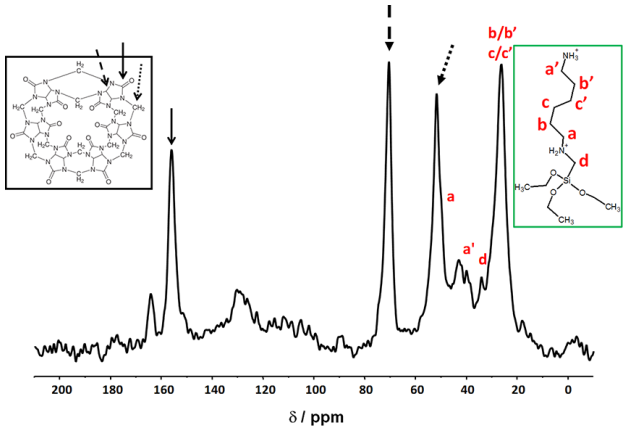

Fig. 8 CP-MAS ^{13}C NMR spectrum of NS@mSi-valve

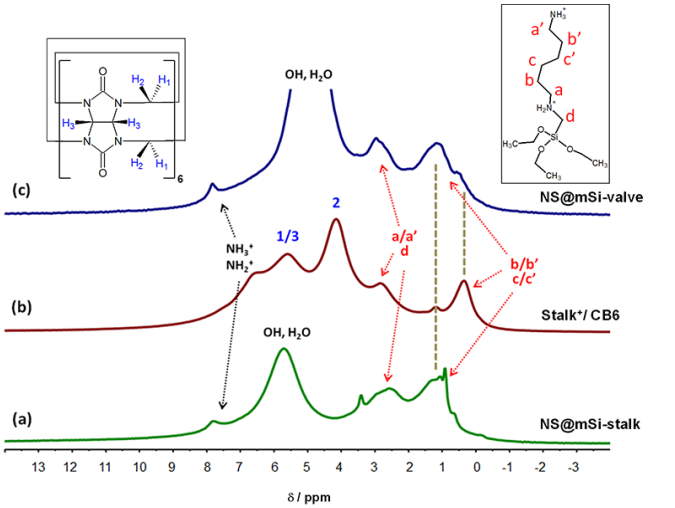

Fig. 9 ^{1}H MAS (V_r = 60 kHz) spectra of a) NS@mSi-stalk, b) stalk^{+}/CB6 and c) NS@mSi-valve

Then, the presence of CB6 in the NS@mSi-valve can be straightforwardly identified in the spectrum thanks to the characteristic peaks at 51.8, 70.5 and 156.1 ppm corresponding to the resonances of CH_2, CH and C=O moieties respectively according to CP-MAS ^{13}C spectrum of CB6 (see Fig. S7). Additional peaks located at 131 and 165 ppm are due to impurities. Finally, these results confirm the presence of stalk and CB6 on nanoparticles in agreement with XPS analyses.

Further information regarding the organization of each component can be gained using high speed ^{1}H MAS NMR experiments (60 kHz). Three powder samples have been studied with this technique: NS@mSi-stalk, NS@mSi-valve and the complex stalk^{+}/CB6. The most relevant features that can be identified from the comparison of the stalk^{+}/CB6 reference (Fig. 9b) and of the NS@mSi-stalk (Fig. 9a) are the strong shifts to lower frequencies (≈ - 1 ppm) of the *b*, *b'*, *c*, *c'* CH_2 groups of stalk in the presence of CB6. The shielding of *b*, *b'*, *c*, *c'* CH_2 groups results from the inclusion inside the CB6 cavity and is consistent with the literature data[35] and with our observations by ^{1}H solution-state NMR. A minor peak at ~1.3 ppm remains visible in the stalk^{+}/CB6 spectrum (Fig. 9b) and corresponds to some uncomplexed stalk.

The analysis of the NS@mSi-valve spectrum (Fig. 9c) shows both unshielded and shielded of *b*, *b'*, *c*, *c'* CH_2 resonances for a mixture of complexed and uncomplexed stalk. The shift due to the complexed stalk should also be observed for NH_3^+/NH_2^+ signals as in the spectrum of stalk^{+}/CB6 (Fig. 9b, ≈ 6.6 ppm). However , this resonance is either hidden by the intense SiOH-H_2O peak and/or significantly widened by dipolar coupling with protons of included CB6: the proton–proton dipolar couplings is indeed known to obscure detailed chemical shift information in solid state NMR and reduce spectral resolution.

Additional structural information can be gained by using 2D ^{1}H-^{1}H double quantum MAS experiments which were performed for the three samples (stalk^{+}/CB6, NS@mSi-stalk and NS@mSi-valve) (see Fig. S8-S10†). First, the comparison of the spectra of the three samples clearly shows that DQ coherences of the protons in stalk^{+}/CB6 (correlation spots A, C, D, E, F, I and J) and in NS@mSi-stalk (correlation spots B, C, G, H, K, L, M and N) can also be found in the spectrum of NS@mSi-valve.

These results unambiguously demonstrate that the two situations (bound and unbound to CB6) exist for the grafted stalk. Additionally, an estimation of the proportion of stalk molecules in each configuration can be made. The assessment of the area of characteristic correlations (A and B DQ coherence area corresponding to the *b*/*b'*/*c*/*c'* methylene groups for stalk forming complex with CB6 vs. uncomplexed stalk respectively) gives a 1:3 ratio. The presence of stalk molecules that are not interacting with CB6 could be the result of the interaction of the amine group of stalk with surface silanols via hydrogen bonds and would prevent inclusion. This assumption is indeed supported by CP-MAS ^{13}C spectrum (Fig. 8) and the presence of several resonances for *a'* that indicates at least two structural forms for the stalk molecule.[16,31,45]

Conclusion

This work provides a detailed study about the physico-chemical characterization of a model mechanized silver-gold alloy@mesoporous silica shell/pseudorotaxane nano-assembly using two main complementary techniques: XPS and solution- and solid-state NMR. The originality of such complementarity comes from the combination of both surface and volume spectroscopic detection techniques with high sensitivity. Such association is particularly suitable and adapted to the study of hybrid stimulus-responsive interfaces for which the identification and the quantification of organic and inorganic entities have to be determined in relation with their multiple hard and soft chemical interactions.

The introduction of stalk in the silica network was clearly demonstrated as the Si2p peak shifts to the low energy side after grafting while C1s and N1s core peaks have evidenced the presence of CB6 onto nanoparticles surface. For the first time, the complex formation on nanoparticles was proved by high speed ^{1}H MAS NMR experiments. Actually, the low frequency shift of the aliphatic protons of stalk, usually seen in

liquid state ^{1}H NMR, was also revealed in the solid state NMR study. However, these ^{1}H solid state NMR experiments have also pointed out that the majority of the stalk is not in interaction with CB6 macrocycles, when formulated in powder after removing the solvent. This can be related to the large number of possible organizations of the stalk grafted onto the silica surface (isolated molecule or oligomers (closely packed)). Indeed, one key point of such nano-assembly design is to clearly understand how the stalk is grafted onto the nanoparticles, depending on the different synthesis parameters such as the nature of the solvent, the temperature, the silane concentration and also the ambient humidity. [46,47] Furthermore, CB6 may also interact with silanols via hydrogen-bonding[48] which increase the number of possible assemblies: complexation of stalk and CB6, amine groups of stalk interacting with silanols, carbonyl groups of CB6 interacting with silanols… Moreover, further experiments have to be carried out especially in solid state NMR on functionalized nanoparticles dispersed in solution, as the dynamics of molecules may be different than in powder.

Finally, these nano-assemblies with a gold nanoshell core appear more promising than mechanized gold@silica nanoparticles, as their hollow shape involves a plasmon resonance in the NIR region, which is more biologically relevant. Smaller systems (~100nm diameter) are now envisaged and tested for better fit to endocytosis of cells for use in nanomedicine.

Acknowledgements

We thanks Arkema for the TEM analyses and CNRS and Region Aquitaine for their financial supports.

Notes and references

1 M. Vallet-Regi, A. Rámila, R. P. del Real and J. Pérez-Pariente, *Chem. Mater.*, 2001, **13**, 308–311.
2 C. Argyo, V. Weiss, C. Bräuchle and T. Bein, *Chem. Mater.*, 2014, **26**, 435–451.
3 M. W. Ambrogio, C. R. Thomas, Y.-L. Zhao, J. I. Zink and J. F. Stoddart, *Acc. Chem. Res.*, 2011, **44**, 903–913.
4 S. Saha, K. C.-F. Leung, T. D. Nguyen, J. F. Stoddart and J. I. Zink, *Adv. Funct. Mater.*, 2007, **17**, 685–693.
5 J. Liu, X. Du and X. Zhang, *Chem. – Eur. J.*, 2011, **17**, 810–815.
6 J. Liu and X. Du, *J. Mater. Chem.*, 2010, **20**, 3642–3649.
7 O. C. Farokhzad and R. Langer, *Adv. Drug Deliv. Rev.*, 2006, **58**, 1456–1459.
8 S. S. Kelkar and T. M. Reineke, *Bioconjug. Chem.*, 2011, **22**, 1879–1903.
9 J. Xie, S. Lee and X. Chen, *Adv. Drug Deliv. Rev.*, 2010, **62**, 1064–1079.
10 S. M. Janib, A. S. Moses and J. A. MacKay, *Adv. Drug Deliv. Rev.*, 2010, **62**, 1052–1063.
11 N.-T. Chen, S.-H. Cheng, J. S. Souris, C.-T. Chen, C.-Y. Mou and L.-W. Lo, *J. Mater. Chem. B*, 2013, **1**, 3128.
12 J. Croissant and J. I. Zink, *J. Am. Chem. Soc.*, 2012, **134**, 7628–7631.
13 S. Soulé, J. Allouche, J.-C. Dupin and H. Martinez, *Microporous Mesoporous Mater.*, 2013, **171**, 72–77.
14 S. Angelos, Y.-W. Yang, K. Patel, J. F. Stoddart and J. I. Zink, *Angew. Chem. Int. Ed.*, 2008, **47**, 2222–2226.
15 S. Zhou, H. Sha, X. Ke, B. Liu, X. Wang and X. Du, *Chem. Commun.*, 2015, **51**, 7203–7206.
16 M. Wang, T. Chen, C. Ding and J. Fu, *Chem. Commun.*, 2014, **50**, 5068–5071.
17 J. Fu, T. Chen, M. Wang, N. Yang, S. Li, Y. Wang and X. Liu, *ACS Nano*, 2013, **7**, 11397–11408.
18 X. Huang and X. Du, *ACS Appl. Mater. Interfaces*, 2014, **6**, 20430–20436.
19 C. R. Thomas, D. P. Ferris, J.-H. Lee, E. Choi, M. H. Cho, E. S. Kim, J. F. Stoddart, J.-S. Shin, J. Cheon and J. I. Zink, *J Am Chem Soc*, 2010, **132**, 10623–10625.
20 S. Brunauer, P. H. Emmett and E. Teller, *J. Am. Chem. Soc.*, 1938, **60**, 309–319.
21 P. I. Ravikovitch and A. V. Neimark, *J. Phys. Chem. B*, 2001, **105**, 6817–6823.
22 D. A. Shirley, *Phys. Rev. B*, 1972, **5**, 4709.
23 J. H. Scofield, *J. Electron Spectrosc. Relat. Phenom.*, 1976, **8**, 129–137.
24 W. Sommer, J. Gottwald, D. E. Demco and H. W. Spiess, *J. Magn. Reson. A*, 1995, **113**, 131–134.
25 J. B. Ledeuil, A. Uhart, S. Soulé, J. Allouche, J. C. Dupin and H. Martinez, *Nanoscale*, 2014, **6**, 11130–11140.
26 T. Gross, M. Ramm, H. Sonntag, W. Unger, H. M. Weijers and E. H. Adem, *Surf. Interface Anal.*, 1992, **18**, 59–64.
27 M. L. Miller and R. W. Linton, *Anal. Chem.*, 1985, **57**, 2314–2319.
28 K. M. R. Kallury, U. J. Krull and M. Thompson, *Anal. Chem.*, 1988, **60**, 169–172.
29 P. R. Moses, L. M. Wier, J. C. Lennox, H. O. Finklea, J. R. Lenhard and R. W. Murray, *Anal. Chem.*, 1978, **50**, 576–585.
30 B. Kannan, D. A. Higgins and M. M. Collinson, *Langmuir*, 2012, **28**, 16091–16098.
31 G. S. Caravajal, D. E. Leyden, G. R. Quinting and G. E. Maciel, *Anal. Chem.*, 1988, **60**, 1776–1786.
32 F. Zhang and M. P. Srinivasan, *Langmuir*, 2004, **20**, 2309–2314.
33 K. M. R. Kallury, P. M. Macdonald and M. Thompson, *Langmuir*, 1994, **10**, 492–499.
34 C. Márquez, R. R. Hudgins and W. M. Nau, *J. Am. Chem. Soc.*, 2004, **126**, 5806–5816.
35 E. Masson, X. Lu, X. Ling and D. L. Patchell, *Org. Lett.*, 2009, **11**, 3798–3801.
36 L. Leclercq, N. Noujeim, S. H. Sanon and A. R. Schmitzer, *J. Phys. Chem. B*, 2008, **112**, 14176–14184.
37 N. Noujeim, L. Leclercq and A. R. Schmitzer, *J. Org. Chem.*, 2008, **73**, 3784–3790.
38 S. Samsam, L. Leclercq and A. R. Schmitzer, *J. Phys. Chem. B*, 2009, **113**, 9493–9498.
39 J. Lagona, P. Mukhopadhyay, S. Chakrabarti and L. Isaacs, *Angew. Chem. Int. Ed.*, 2005, **44**, 4844–4870.
40 W. L. Mock and N. Y. Shih, *J. Org. Chem.*, 1986, **51**, 4440–4446.
41 L. Fusaro, E. Locci, A. Lai and M. Luhmer, *J. Phys. Chem. B*, 2008, **112**, 15014–15020.
42 A. Cros-Gagneux, F. Delpech, C. Nayral, A. Cornejo, Y. Coppel and B. Chaudret, *J. Am. Chem. Soc.*, 2010, **132**, 18147–18157.
43 H. Virieux, M. Le Troedec, A. Cros-Gagneux, W.-S. Ojo, F. Delpech, C. Nayral, H. Martinez and B. Chaudret, *J. Am. Chem.*

Soc., 2012, **134**, 19701–19708.

44 A. Cornejo, G. Fuks, V. Martínez-Merino, Í. Sarobe, M. J. Gil, K. Philippot, B. Chaudret, F. Delpech and C. Nayral, *New J Chem*, 2014, **38**, 6103–6113.
45 C. Chiang, N.-I. Liu and J. L. Koenig, *J. Colloid Interface Sci.*, 1982, **86**, 26–34.
46 M. Zhu, M. Z. Lerum and W. Chen, *Langmuir*, 2012, **28**, 416–423.
47 K. K. Sharma, A. Anan, R. P. Buckley, W. Ouellette and T. Asefa, *J. Am. Chem. Soc.*, 2008, **130**, 218–228.
48 L. Ma, S. Liu, Q. Wang, L. Yao and L. Xu, *J. Sep. Sci.*, 2015, **38**, 1082–1089.